

Predicting drug-induced arrhythmias by multiscale modeling

Francisco Sahli Costabal¹ | Jiang Yao² | Ellen Kuhl³ 

¹Department of Mechanical Engineering, Stanford University, Stanford, CA, USA

²Dassault Systèmes Simulia Corporation, Johnston, RI, USA

³Departments of Mechanical Engineering, Bioengineering, and Cardiothoracic Surgery, Stanford University, Stanford, CA, USA

Correspondence

Ellen Kuhl, Departments of Mechanical Engineering, Bioengineering, and Cardiothoracic Surgery, Stanford University, 452 Escondido Mall, Building 520-203, Stanford, CA 94305, USA.
Email: ekuhl@stanford.edu

Funding information

National Institutes of Health, Grant/Award Number: U01 HL119578

Abstract

Drugs often have undesired side effects. In the heart, they can induce lethal arrhythmias such as torsades de pointes. The risk evaluation of a new compound is costly and can take a long time, which often hinders the development of new drugs. Here, we establish a high-resolution, multiscale computational model to quickly assess the cardiac toxicity of new and existing drugs. The input of the model is the drug-specific current block from single cell electrophysiology; the output is the spatio-temporal activation profile and the associated electrocardiogram. We demonstrate the potential of our model for a low-risk drug, ranolazine, and a high-risk drug, quinidine: For ranolazine, our model predicts a prolonged QT interval of 19.4% compared with baseline and a regular sinus rhythm at 60.15 beats per minute. For quinidine, our model predicts a prolonged QT interval of 78.4% and a spontaneous development of torsades de pointes both in the activation profile and in the electrocardiogram. Our model reveals the mechanisms by which electrophysiological abnormalities propagate across the spatio-temporal scales, from specific channel blockage, via altered single cell action potentials and prolonged QT intervals, to the spontaneous emergence of ventricular tachycardia in the form of torsades de pointes. Our model could have important implications for researchers, regulatory agencies, and pharmaceutical companies on rationalizing safe drug development and reducing the time-to-market of new drugs.

KEYWORDS

arrhythmia, cardiac toxicity, drugs, electrophysiology, finite element analysis, torsades de pointes

1 | INTRODUCTION

Drugs of many types can induce global changes in cardiac electrophysiology by interacting with specific ionic channels. Undesirable side effect of some compounds is cardiac arrhythmias. A particularly lethal type of arrhythmia is torsades de pointes,¹ a condition associated with drugs that prolong the repolarization stage of the action potential.² The current gold standard to assess the pro-arrhythmic risk of a drug is to measure the block of the rapid delayed potassium rectifier current in single cell experiments,³ the QT interval in animal models, and the corrected QT interval in healthy volunteers.⁴ Pro-arrhythmic risk evaluation is critical to avoid the introduction of potentially dangerous drugs to the market.⁵ Yet the high cost and long time needed to test new compounds hinder the discovery of new drugs. In addition, the poor specificity of these markers can prevent potentially useful drugs to reach the market.

A promising initiative is the Comprehensive in vitro Proarrhythmia Assay (CiPA) that brings together regulatory agencies, industry, and researchers to establish new mechanistic assays that can predict the pro-arrhythmic risk of new compounds.⁶ A major recommendation of the CiPA initiative is to promote computational models⁷ to quantify the effect of drugs.⁸ Ideally, these models can quickly evaluate the impact of a new drug on the predictive biomarkers of cardiac arrhythmias: In a single cell model, a recent study characterized the prolongation in action potential duration and predicted the risk categories of 31 drugs.⁹ In a one-dimensional model of cardiac electrophysiology, other studies computed alterations in the QT interval in response to drugs.^{10,11} In a three-dimensional model, a recent study identified critical drug concentrations for cardiac arrhythmias and correlated these concentrations to risk categories of torsades de pointes.¹² However, there are still many open questions that could benefit from high-fidelity modeling.⁷ Arrhythmias are inherently three-dimensional phenomena. Multiscale modeling could allow us to mechanistically correlate what a pharmacologist sees in a single cell action potential to what a physician sees in a clinical electrocardiogram. Towards this goal, we establish a multiscale biventricular model to characterize the effects of drugs in cardiac electrophysiology. Our model allows us to quantify the interaction between specific compounds and specific ionic currents at the cellular scale and compute the overall response in terms of global activation profiles and electrocardiograms at the organ scale.

We hypothesize that drugs with mild effects will produce moderate changes in the electrocardiogram, whereas in high-risk drugs will trigger the spontaneous development of arrhythmias. We test this hypothesis for two common approved drugs with well-known risk factors, ranolazine and quinidine. Ranolazine was approved a decade ago as a drug to treat chronic angina.¹³ It blocks the rapid delayed potassium rectifier current and the late component of the sodium current.¹⁴ Although ranolazine is known to moderately prolong the action potential duration and QT interval, it has been classified with a low risk of torsades de pointes.⁸ Quinidine was discovered more than a century ago as a drug to treat cardiac arrhythmias.¹⁵ It blocks the rapid and slow delayed potassium rectifier currents and the transient outward potassium current.¹⁴ Quinidine is known to significantly increase the action potential duration and the QT interval, which has led to its classification with a high risk of torsades de pointes.³ Here, we show how ranolazine- and quinidine-induced alterations in ion channel dynamics propagate across the spatial and temporal scales to modify the action potential duration on the cellular level, the QT interval on the organ level, and the excitation pattern across the left and right ventricles. We anticipate that our multiscale computational model will become a useful tool to better understand the mechanisms of drug-induced arrhythmias and accelerate the development of new compounds.

2 | METHODS

2.1 | Cardiac electrophysiology

We represent the electrophysiology of cardiac tissue by the classical monodomain model. The key variable of the monodomain model is the transmembrane potential ϕ , the difference between the intracellular and extracellular potentials. The spatio-temporal evolution of the transmembrane potential is governed by a reaction-diffusion equation,¹⁶

$$\chi (C_m \dot{\phi} + I_{\text{ion}}) = \text{div}(\hat{\mathbf{D}} \cdot \nabla \phi), \quad (1)$$

where χ is the surface-to-volume ratio of the cell, C_m is the membrane capacitance, I_{ion} is the ionic current across the cell membrane, and $\hat{\mathbf{D}}$ is the second-order conductivity tensor.¹⁷ By normalizing this equation with (χC_m) , we obtain the classical format of the evolution equation for the transmembrane potential in cardiac tissue,

$$\dot{\phi} = \text{div}(\mathbf{D} \cdot \nabla \phi) + f^\phi. \quad (2)$$

Here, we have introduced the source term $f^\phi = -I_{\text{ion}}/C_m$ and the new conductivity tensor \mathbf{D} , which we further decompose into isotropic and anisotropic contributions,

$$\mathbf{D} = \frac{1}{\chi C_m} \hat{\mathbf{D}} = D_{\text{iso}} \mathbf{I} + D_{\text{ani}} \mathbf{f} \otimes \mathbf{f}, \quad (3)$$

to account for the anisotropy of cardiac tissue in terms of the orientation \mathbf{f} of the cardiac muscle fibers.¹⁸ A wealth of research has focused understanding single cell dynamics and characterizing the ionic currents I_{ion} of different cell types.¹⁹ In general, the currents are functions of the transmembrane potential ϕ and a set of states variables $\mathbf{q}(\phi)$,^{20,21}

$$I_{\text{ion}} = I_{\text{ion}}(\phi, \mathbf{q}(\phi); t), \quad (4)$$

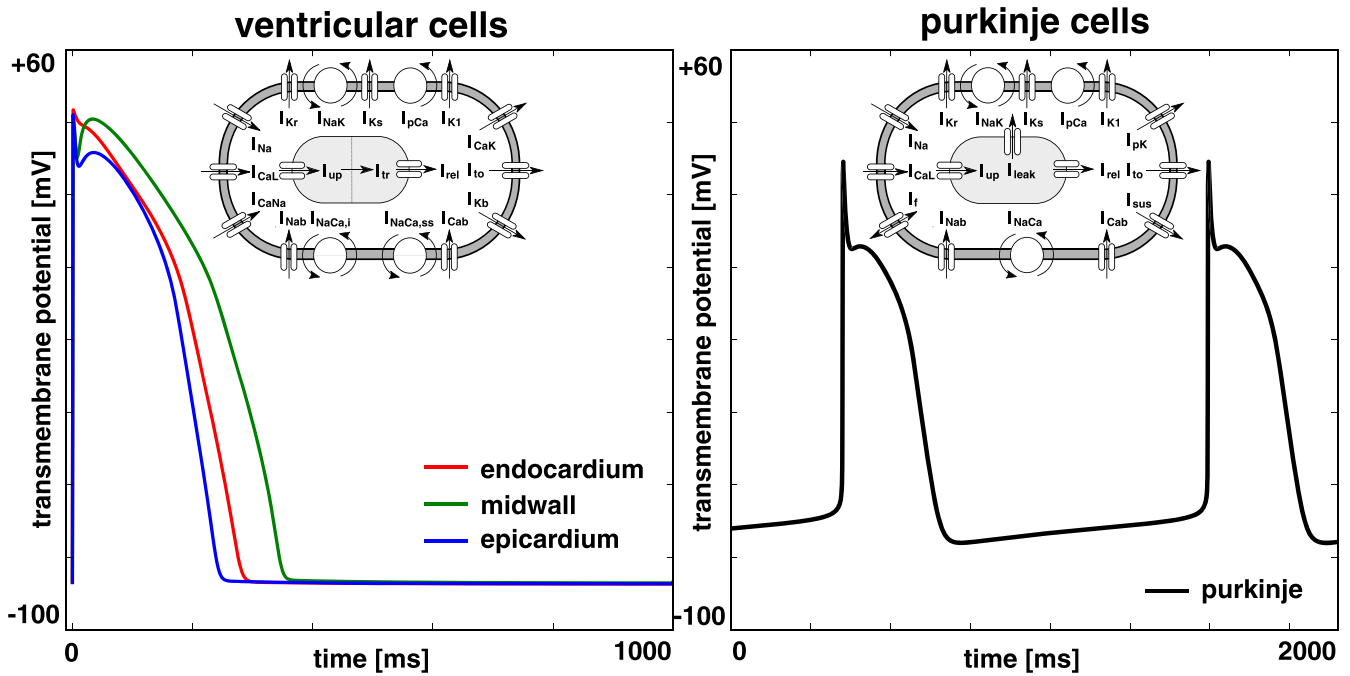


FIGURE 1 Single cell action potential for human ventricular cardiomyocytes, left, and Purkinje fiber cells, right. The ventricular cell model distinguishes between endocardial, midwall, and epicardial cells and is based on the modified O'Hara-Rudy model with 15 ionic currents and 39 state variables.²² The Purkinje cell model displays inherent automaticity and is based on the Stewart model with 14 ionic currents and 20 state variables²⁶

where the state variables themselves are governed by ordinary differential equations,

$$\dot{\mathbf{q}} = \mathbf{g}(\phi, \mathbf{q}(\phi); t). \quad (5)$$

The number of currents and state variables determines the complexity of the model and varies for different cell types. Here, we selected two distinct cell models, one for human ventricular cardiomyocytes and one for Purkinje fiber cells.

2.1.1 | Ventricular cardiomyocyte model

To model the electrophysiology of ventricular cells, we adopt the O'Hara-Rudy model for human ventricular cardiomyocytes.²² The O'Hara-Rudy model was developed exclusively based on human data; it includes the key currents relevant in drug-induced arrhythmias, and it is recommended by the CiPA initiative to unify regulatory guidelines.²³ The model is based on 15 ionic currents,

$$I_{\text{ion}} = I_{\text{CaL}} + I_{\text{Na}} + I_{\text{CaNa}} + I_{\text{CaK}} + I_{\text{Cab}} + I_{\text{Nab}} + I_{\text{Kb}} + I_{\text{Kr}} + I_{\text{Ks}} + I_{\text{K1}} + I_{\text{to}} + I_{\text{NaK}} + I_{\text{pCa}} + I_{\text{NaCa,i}} + I_{\text{NaCa,ss}}, \quad (6)$$

the L-type calcium current I_{CaL} ; the fast and late sodium currents I_{Na} ; the calcium sodium and calcium potassium currents I_{CaNa} and I_{CaK} ; the background calcium, sodium, and potassium currents I_{Cab} , I_{Nab} , and I_{Kb} ; the rapid and slow delayed rectifier potassium currents I_{Kr} and I_{Ks} ; the inward rectifier potassium current I_{K1} ; the transient outward potassium current I_{to} ; the sodium potassium pump current I_{NaK} ; the sarcolemmal calcium pump current I_{pCa} ; and the sodium calcium exchange currents $I_{\text{NaCa,i}}$ and $I_{\text{NaCa,ss}}$. Here, we replaced the fast sodium current I_{Na} of the original O'Hara-Rudy model with a modified fast sodium current of the ten Tusscher model²⁴ to model propagation in tissue scale simulations.²⁵ The 15 currents are defined through a total of 39 state variables. This level of detail is suitable to study the interaction of specific drugs across specific ionic channels. To account for regional specificity, the O'Hara-Rudy model has been parameterized for 3 different cell types, endocardial, midwall, and epicardial cells. Figure 1, left, illustrates the single cell action potential of the O'Hara-Rudy model for endocardial, mid, and epicardial human ventricular cardiomyocytes. We adopted the code of the original O'Hara-Rudy model,²⁷ translated it to Fortran, replaced the fast sodium current,²⁴ and kept all the parameters as in the original model.²²

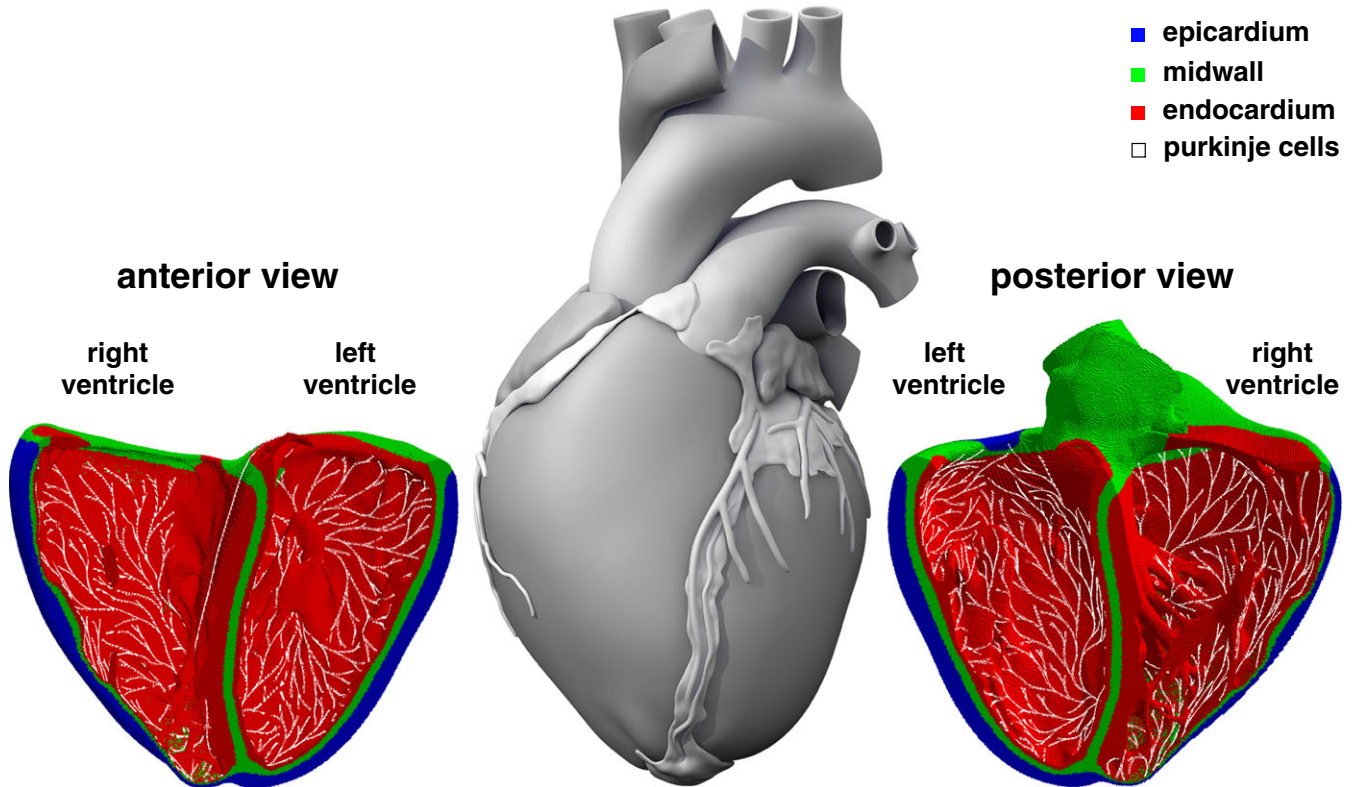


FIGURE 2 Finite element model of the left and right ventricles created from high-resolution magnetic resonance images of a human heart.³¹ The ventricular wall is discretized with 6 878 459 regular linear hexagonal finite elements with an edge length of 0.3 mm, a total number of 7 519 918 nodes, and 268 259 901 internal variables. The Purkinje fiber network is discretized with 39 772 linear cable elements, a total number of 39 842 nodes, and 795 440 internal variables. It is connected to the ventricles at its terminals through 3545 resistor elements. Epicardial, midwall, and endocardial cells are marked in blue, green, and red; Purkinje cells are shown in white

2.1.2 | Purkinje fiber model

To model the electrophysiology of the Purkinje fiber network, we choose the Stewart model for human Purkinje fiber cells.²⁶ A characteristic feature of this model is the automaticity of its action potential, which enables the cells to self-excite without an external stimulus. This model is based on 14 ionic currents,

$$I_{\text{ion}} = I_{\text{CaL}} + I_{\text{Na}} + I_{\text{Cab}} + I_{\text{Nab}} + I_{\text{Kr}} + I_{\text{Ks}} + I_{\text{K1}} + I_{\text{to}} + I_{\text{f}} + I_{\text{sus}} + I_{\text{NaK}} + I_{\text{pCa}} + I_{\text{pK}} + I_{\text{NaCa}}, \quad (7)$$

the L-type calcium current I_{CaL} , the fast and late sodium currents I_{Na} , the background calcium and sodium currents I_{Cab} and I_{Nab} , the rapid and slow delayed rectifier potassium currents I_{Kr} and I_{Ks} , the inward rectifier potassium current I_{K1} , the transient outward potassium current I_{to} , the hyperpolarization-activated current I_{f} , the sustained potassium current I_{sus} , the sodium potassium pump current I_{NaK} , the calcium and potassium pump currents I_{pCa} and I_{pK} , and the sodium calcium exchange current I_{NaCa} . These currents are defined through 20 state variables. Figure 1, right, illustrates the single cell action potential for human Purkinje cells. We adopted the code of the original Stewart model,²⁸ translated it to Fortran, and kept all the parameters as in the original model.²⁶

2.2 | Finite element model

To solve the governing Equations 2 to 5, we adopt the finite element software package Abaqus.²⁹ We exploit the structural similarities with the heat transfer problem with a nonlinear heat source and discretize the transmembrane potential as nodal degree of freedom and the ionic currents and gating variables as internal variables.^{18,30} Motivated by the small time step size to resolve the fast dynamics during the initial phase of the action potential, we adopt an explicit time integration scheme.

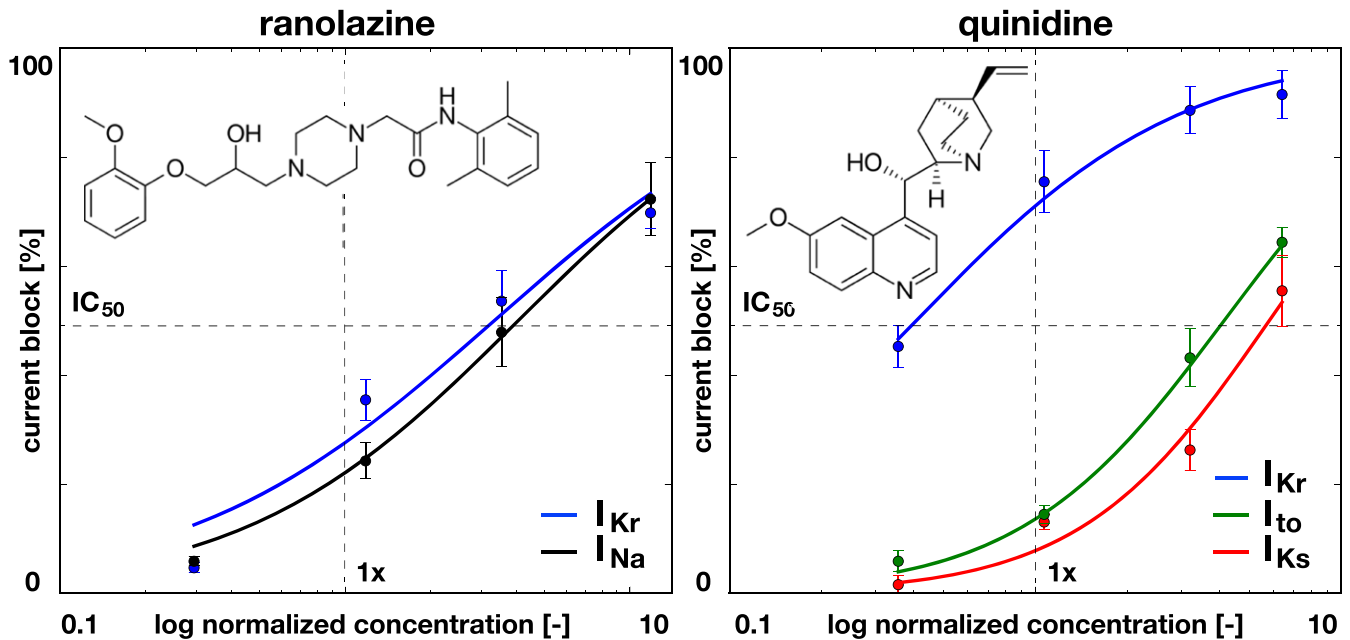


FIGURE 3 Effects of ranolazine and quinidine on different ionic currents. Ranolazine primarily blocks the rapid delayed rectifier potassium current I_{Kr} and the late component of the sodium current I_{Na} ; quinidine primarily blocks the rapid and slow delayed rectifier potassium currents I_{Kr} and I_{Ks} and the transient outward potassium current I_{to} . The concentration is plotted on a logarithmic scale and normalized with respect to the free plasma concentrations of ranolazine, 1948.2 nM, and quinidine, 842.9 nM, dashed vertical lines at $1\times$. Solid lines represent the fitted Hill model; error bars represent the standard error mean¹⁴

2.2.1 | Ventricular tissue model

The basis for our simulation is the Living Heart model, an anatomically accurate 4-chamber model of the healthy human heart.³³ The underlying anatomic model was created from magnetic resonance images of a healthy, 21-year-old, 50th percentile US male.³¹ Its images were reconstructed from 0.75-mm-thick slices using a medium soft-tissue kernel with retrospective electrocardiogram gating. The initial DICOM images were exported as JPEG files, segmented using Amira, postprocessed using Maya, and converted into NURBS surfaces, from which the final solid model was created.³² Motivated by the relationship between element size and critical time step size in explicit methods, we converted this geometry into a regular discretization of cube elements with a constant edge length of 0.3 mm across the entire domain. This results in a discretization with 6 878 459 regular linear hexagonal finite elements, 7 519 918 nodes, and 268 259 901 internal variables. For the flux term, we include tissue anisotropy using the fiber definitions \mathbf{f} of the Living Heart model³³ and choose the isotropic and anisotropic conductivities to $D_{iso} = 0.012 \text{ mm}^2/\text{ms}$ and $D_{ani} = 0.078 \text{ mm}^2/\text{ms}$.¹⁷ For the source term, we use a body flux subroutine to incorporate the ionic currents I_{ion} in the solid element formulation.²⁹ To account for regional specificity in cell type, we simulate a series of Laplace problems using the ventricular model with 3 sets of essential boundary conditions, at the epicardial surface, at the left endocardial surface, and at the right endocardial surface.³⁴ The combination of boundary conditions defines transmural gradients according to which we allocate the different cell types, 20% endocardial, 30% midwall, and 50% epicardial cells. This arrangement ensures positive T waves in the healthy baseline electrocardiogram.³⁵ Figure 2 illustrates the underlying human heart anatomy and the finite element model of the left and right ventricles with the epicardial, midwall, and endocardial cells are marked in blue, green, and red and the Purkinje fiber network shown in white.

2.2.2 | Purkinje network model

The inclusion of the Purkinje network is critical to model correct excitation patterns. We create the network as fractal tree that grows on the endocardial surface.³⁶ By construction, branches of the tree repel one another and follow the gradient of the distance of all existing branches. We initialize tree growth at 4 anatomical locations, the right bundle branch, the left bundle branch, and the anterior and posterior fascicles of the left ventricle. The right ventricular septum is not covered by the Purkinje network since this region is known to activate from left to right. This results in a discretization with 39 772 linear cable elements, 39 842 nodes, and 795 440 internal variables. For these Purkinje elements, we developed a

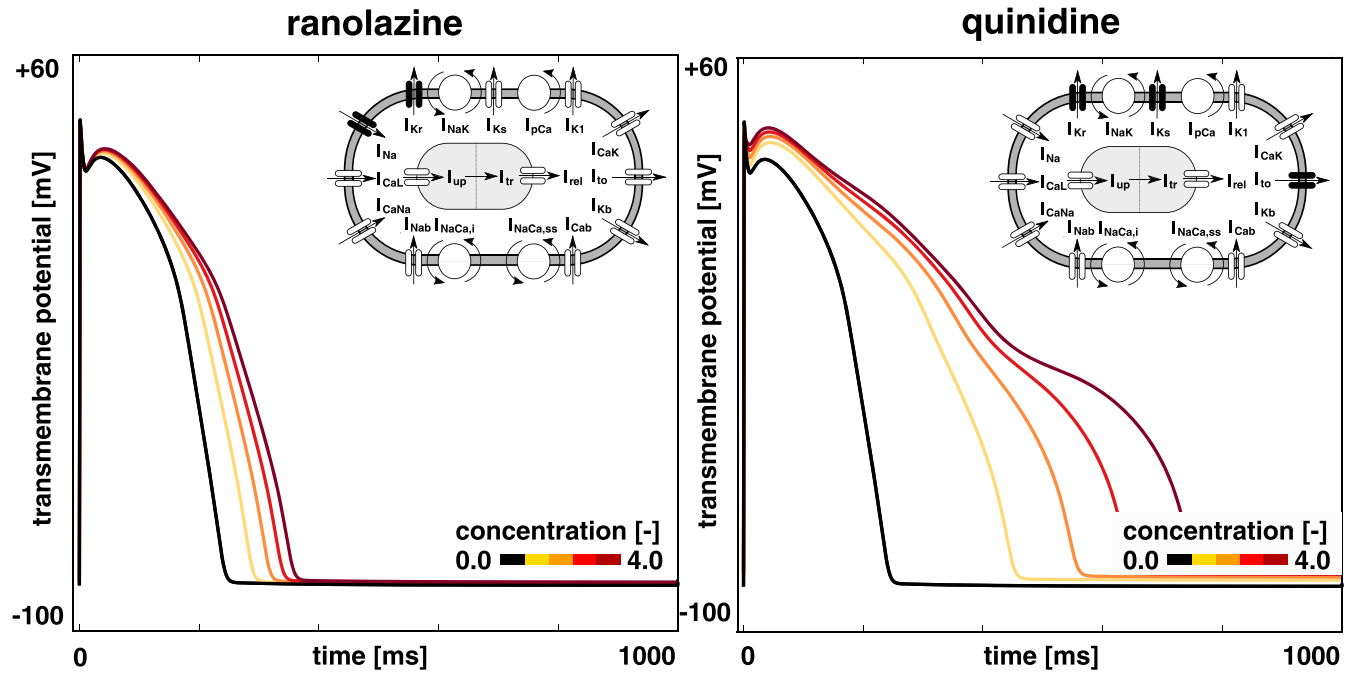


FIGURE 4 Effects of ranolazine and quinidine on single cell action potential. By blocking the rapid delayed rectifier potassium current I_{Kr} and the late component of the sodium current I_{Na} , ranolazine prolongs the plateau of the action potential and moderately increases overall action potential duration. By blocking the rapid and slow delayed rectifier potassium currents I_{Kr} and I_{Ks} and the transient outward potassium current I_{to} , quinidine prolongs the plateau of the action potential and significantly increases overall action potential duration. Black lines represent the baseline action potential of epicardial cells without drugs, yellow to red lines represent the modified action potential for normalized drug concentrations varying between 1 and 4

user element with a discrete version of Equations 2 to 5. We only connect the Purkinje network to the ventricular tissue at the terminals of the fractal tree.³⁷ For these connections, we use 3545 resistor elements with a resistance of $1.78 \Omega\text{m}$, ie, $\chi = 140 \text{ mm}^{-1}$ and $C_m = 0.01 \mu\text{F}/\text{mm}^2$,¹⁷ between each endpoint of the network and the closest node of the ventricular mesh.³⁸ This allows us to adopt distinct cellular models with different resting potentials for ventricular cells and Purkinje cells. Including resistor elements ensures a bidirectional conduction between Purkinje network and surrounding tissue. For the flux term, we choose a conductivity of $D_{\text{iso}} = 3.0 \text{ mm}^2/\text{ms}$. Figure 2 illustrates how densely our discrete Purkinje fiber network covers the endocardium of the left and right ventricles.

2.2.3 | Electrocardiogram Computation

To calculate pseudoelectrocardiograms, at every point $\mathbf{x} \in \mathcal{B}$ across the heart, we project the heart vector, $\nabla\phi$, onto the direction vector, $\nabla(1/|\mathbf{r}|)$, and integrate this projection across the entire cardiac domain \mathcal{B} ,^{16,39}

$$\phi_e(\mathbf{x}_e) = - \int_{\mathcal{B}} \nabla\phi \cdot \nabla \frac{1}{|\mathbf{r}|} dV \quad \text{with} \quad \mathbf{r} = \|\mathbf{x}_e - \mathbf{x}\|. \quad (8)$$

The vector \mathbf{r} points from current point \mathbf{x} to the electrode position \mathbf{x}_e . To mimic one of the precordial leads in the clinical electrocardiogram, we place the electrode 2 cm away from the left ventricular wall. This precordial lead is commonly used to study T waves and QT intervals,⁴⁰ which are critical to assess the risk of drug toxicity.⁴¹

2.3 | Drug model

We model the effect of drugs on single cell action potentials by selectively blocking ionic currents.¹⁴ The degree of block of individual ion channels can be measured experimentally for varying drug concentrations using patch clamp electrophysiology. To estimate the fractional block β for a specific current at any given concentration C , we can fit a Hill-type equation to the discrete data points,

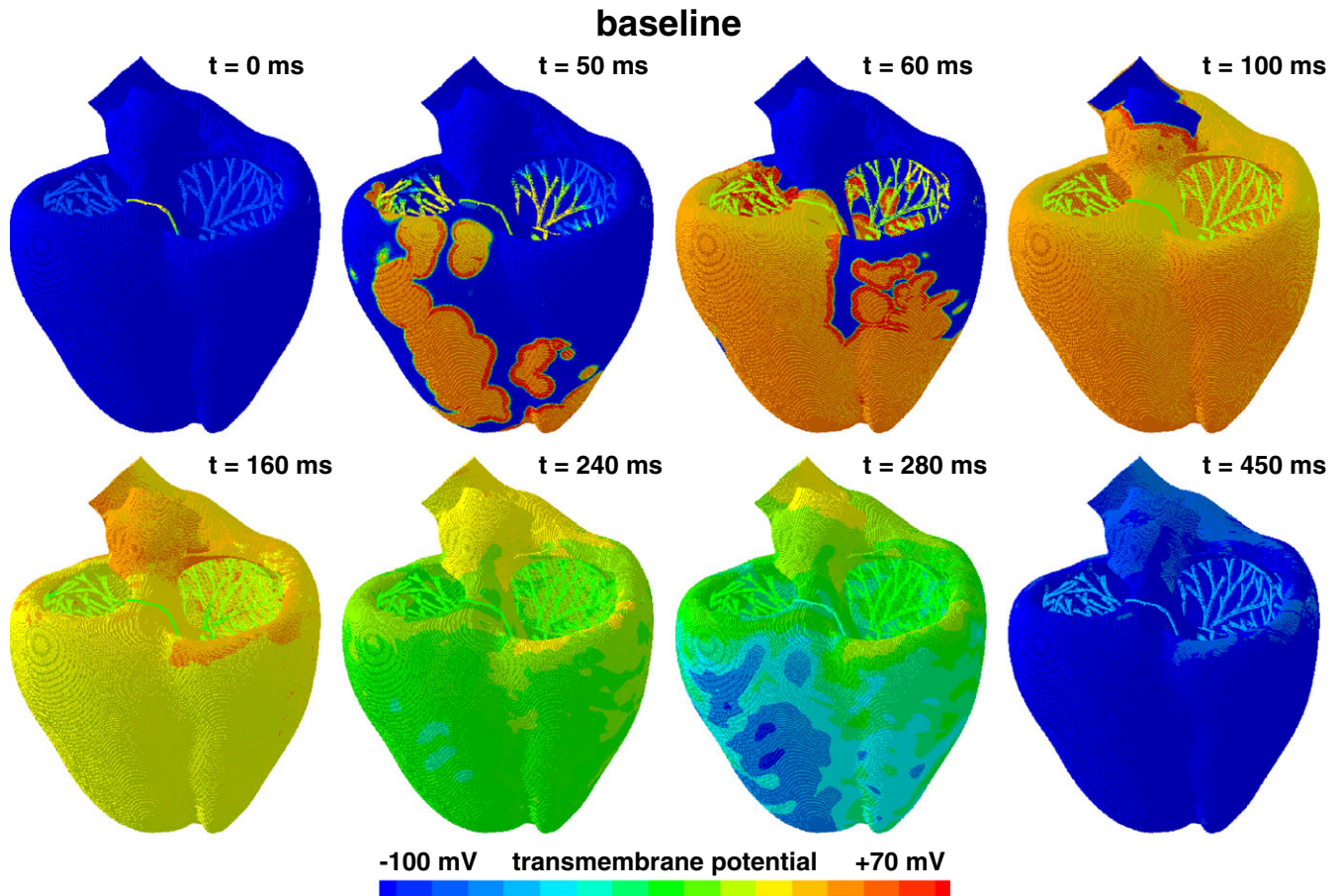


FIGURE 5 Evolution of the transmembrane potential without drugs. Snapshots are taken between the beginning of the QRS complex at 50 milliseconds and the end of the T wave at 450 milliseconds. During depolarization, from 0 to 100 milliseconds, the Purkinje network drives the excitation from apex to base with a sharp depolarization front propagating across the heart. During repolarization, from 100 to 450 milliseconds, both ventricles gradually return to their resting state. The Purkinje network determines the heart rate to 60.15 beats per minute, and the displayed excitation pattern repeats itself identically every 1000 milliseconds, 5 times within the simulated time window of 5000 milliseconds

$$\beta = \frac{C^h}{IC_{50}^h + C^h}. \quad (9)$$

The Hill-type equation has two parameters, the exponent h and the concentration IC_{50} required to achieve a 50% current block. To apply the drug, we scale all affected currents I in all epicardial, midwall, endocardial, and Purkinje cells by the fractional block β of the desired concentration C ,

$$I^{\text{drug}} = [1 - \beta]I. \quad (10)$$

Figure 3 illustrates the effects of the two drugs we consider within this study, ranolazine and quinidine. We follow recommendations by the CiPA initiative¹⁴ and only model the effects on channels that are blocked by 10% and more: Ranolazine primarily blocks the rapid delayed rectifier potassium current I_{Kr} and the late component of the sodium current I_{Na} , and quinidine primarily blocks the rapid and slow delayed rectifier potassium currents I_{Kr} and I_{Ks} and the transient outward potassium current I_{to} . Although ranolazine and quinidine also affect the fast and late sodium currents I_{Na} ,⁴² the L-type calcium current I_{CaL} , and the inward rectifier potassium current I_{K1} , these effects are marginal at the free plasma concentrations we consider in this study.^{9,14,43} The graphs in Figure 3 illustrate the fractional block for varying concentrations, plotted on a logarithmic scale, normalized with respect to the free plasma concentrations of ranolazine, $C_{\text{max}} = 1948.2$ nM, and quinidine, $C_{\text{max}} = 842.9$ nM, as indicated by the dashed vertical lines at $1\times$. The dashed horizontal lines highlight the IC_{50} values. The solid lines represent the fitted Hill model with $h_{Kr} = 0.8$, $IC_{50Kr} = 6490$ nM, $h_{Na} = 0.9$, and $IC_{50Na} = 7884$ nM for ranolazine and $h_{Kr} = 1.0$, $IC_{50Kr} = 343$ nM, $h_{Ks} = 1.3$, $IC_{50Ks} = 3487$ nM, $h_{to} = 4899$, and $IC_{50to} = 1.4$ nM for quinidine; error bars represent the standard error mean.¹⁴

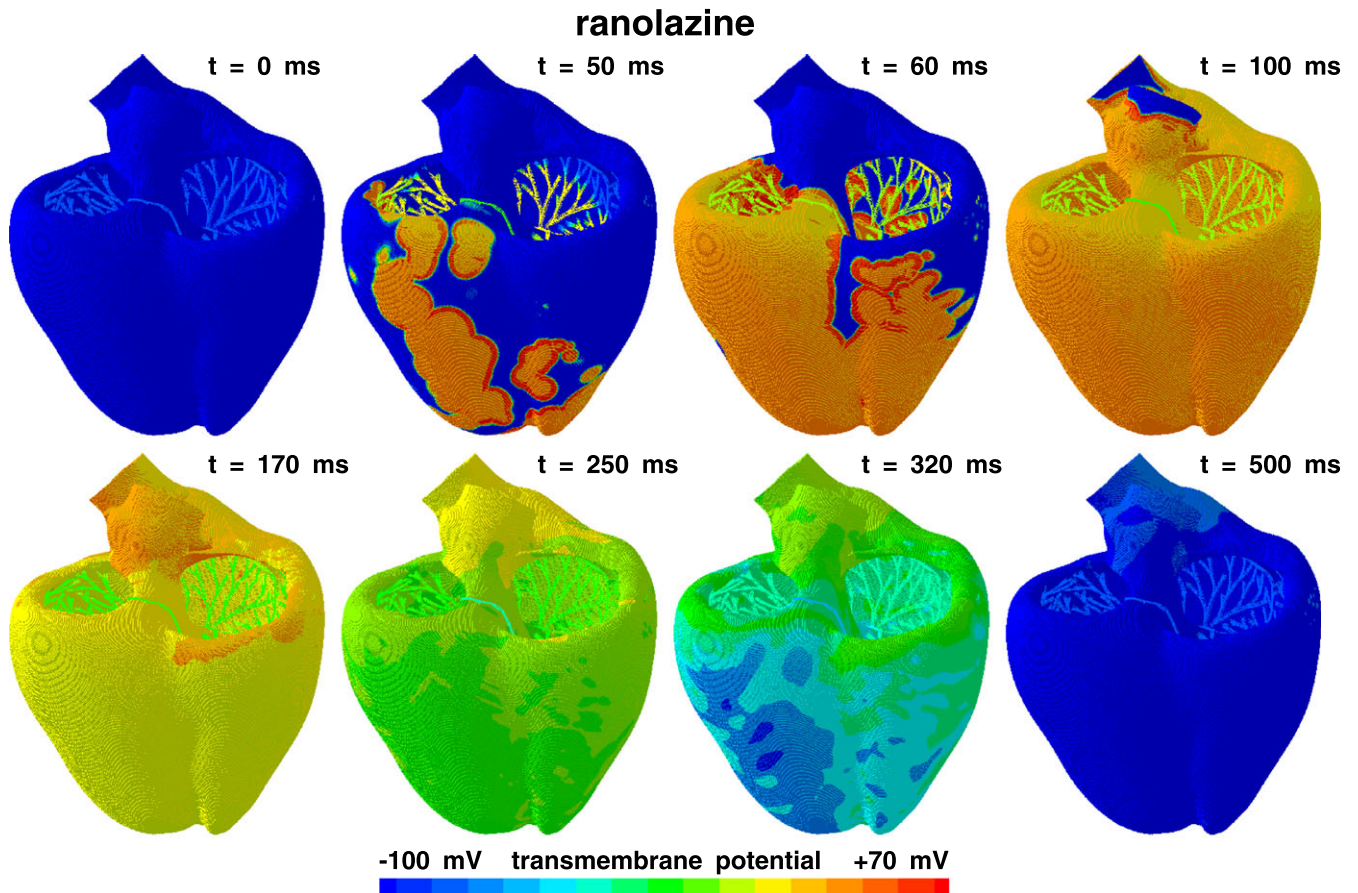


FIGURE 6 Evolution of the transmembrane potential with the drug ranolazine. Snapshots are taken between the beginning of the QRS complex at 50 milliseconds and the end of the T wave at 500 milliseconds. During depolarization, from 0 to 100 milliseconds, the Purkinje network drives the excitation from apex to base with a sharp depolarization front propagating across the heart, almost identical to the case without drugs. During repolarization, from 100 to 500 milliseconds, both ventricles gradually return to their resting state, however, with a delayed repolarization compared with the baseline state. The Purkinje network determines the heart rate to 60.15 beats per minute, and the displayed excitation pattern repeats itself identically every 1000 milliseconds, 5 times within the simulated time window of 5000 milliseconds

Figure 4 illustrates the effects of ranolazine and quinidine on the transmembrane potential. The black lines represent the baseline action potential of epicardial cells without drugs, and the yellow to red lines represent the modified action potential for normalized drug concentrations increasing from 1 to 4. Ranolazine slightly prolongs the plateau of the action potential resulting in a moderate increase of the overall action potential duration. Quinidine markedly prolongs the plateau of the action potential and also increases its peak resulting in a significant increase in overall action potential duration. At similar concentration levels, quinidine has a notably stronger effect on the action potential duration than ranolazine.

3 | RESULTS

To demonstrate the potential of our model, we explore the effects of the drugs ranolazine and quinidine on the activation patterns of the left and right ventricles. We first simulate the baseline electrophysiology without drugs and then apply either ranolazine or quinidine at their free plasma concentrations. In all 3 cases, we simulate a time window of 5000 milliseconds. We initialize the excitation by applying an initial external stimulus at the location of the atrio-ventricular node and then let the automaticity of the Purkinje network drive the following excitation cycles. Figures 5 to 7 show a posterior view of the spatio-temporal evolution of the transmembrane potential for the baseline case and the cases with ranolazine and quinidine. Blue colors represent the resting potential of the heart, and red colors represent the excited state. Figure 8 summarizes the 3 resulting electrocardiograms at the precordial lead.

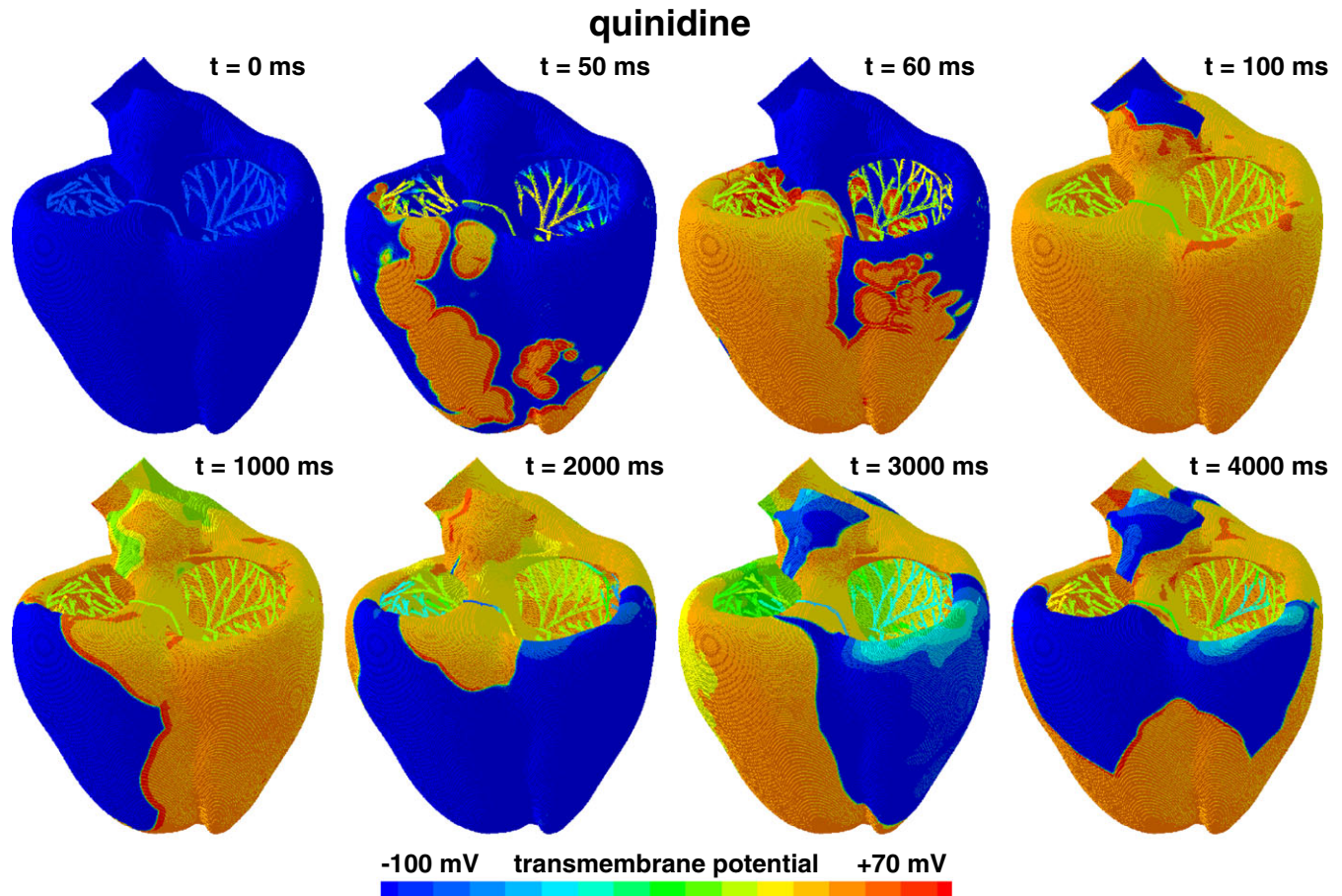


FIGURE 7 Evolution of the transmembrane potential with the drug quinidine. Snapshots are taken at the beginning of the QRS complex at 50 milliseconds, at the end of depolarization at 100 milliseconds, and at every 1000 milliseconds. During the first 100 milliseconds, the Purkinje network drives the excitation from apex to base with a sharp depolarization front propagating across the heart, almost identical to the case without drugs. After a markedly prolonged QT interval, the propagation of the excitation wave becomes irregular and asynchronous. Excitation is no longer driven by the Purkinje network, but by excitation fronts that activate the heart in chaotic patterns, from right to left, from base to apex, from left to right, and from apex to base. These are characteristic features of torsades de pointes

Figure 5 displays the evolution of the transmembrane potential for the baseline case without drugs. The snapshots are taken between the beginning of the QRS complex at 50 milliseconds and the end of the T wave at 450 milliseconds. During depolarization, from 0 to 100 milliseconds, the Purkinje network drives the excitation from apex to base with a sharp depolarization front propagating across the heart. During repolarization, from 100 to 450 milliseconds, both ventricles gradually return to their resting state. The Purkinje network paces the heart at 60.15 beats per minute and the displayed excitation pattern repeats itself identically every 1000 milliseconds, 5 times within the simulated time window of 5000 milliseconds. Figure 8, top row, confirms this observation with regular periodic activation patterns and no signs of arrhythmia. The baseline electrocardiogram displays a well-defined QRS complex and a positive T wave with a QT interval of 257.9 milliseconds.

Figure 6 shows the evolution of the transmembrane potential for the case of ranolazine. The snapshots highlight the beginning of the QRS complex at 50 milliseconds and the end of the T wave at 500 milliseconds. During depolarization, from 0 to 100 milliseconds, the Purkinje network drives the excitation from apex to base with a sharp depolarization front that propagates rapidly across the heart. From Figure 4, left, we know that ranolazine has virtually no effect on the upstroke of the single cell action potential during the first 100 milliseconds of the cardiac cycle. This explains why the depolarization pattern with ranolazine is virtually identical to the baseline case without drugs in Figure 5. During repolarization, from 100 to 500 milliseconds, both ventricles gradually return to their resting state. From Figure 4, left,

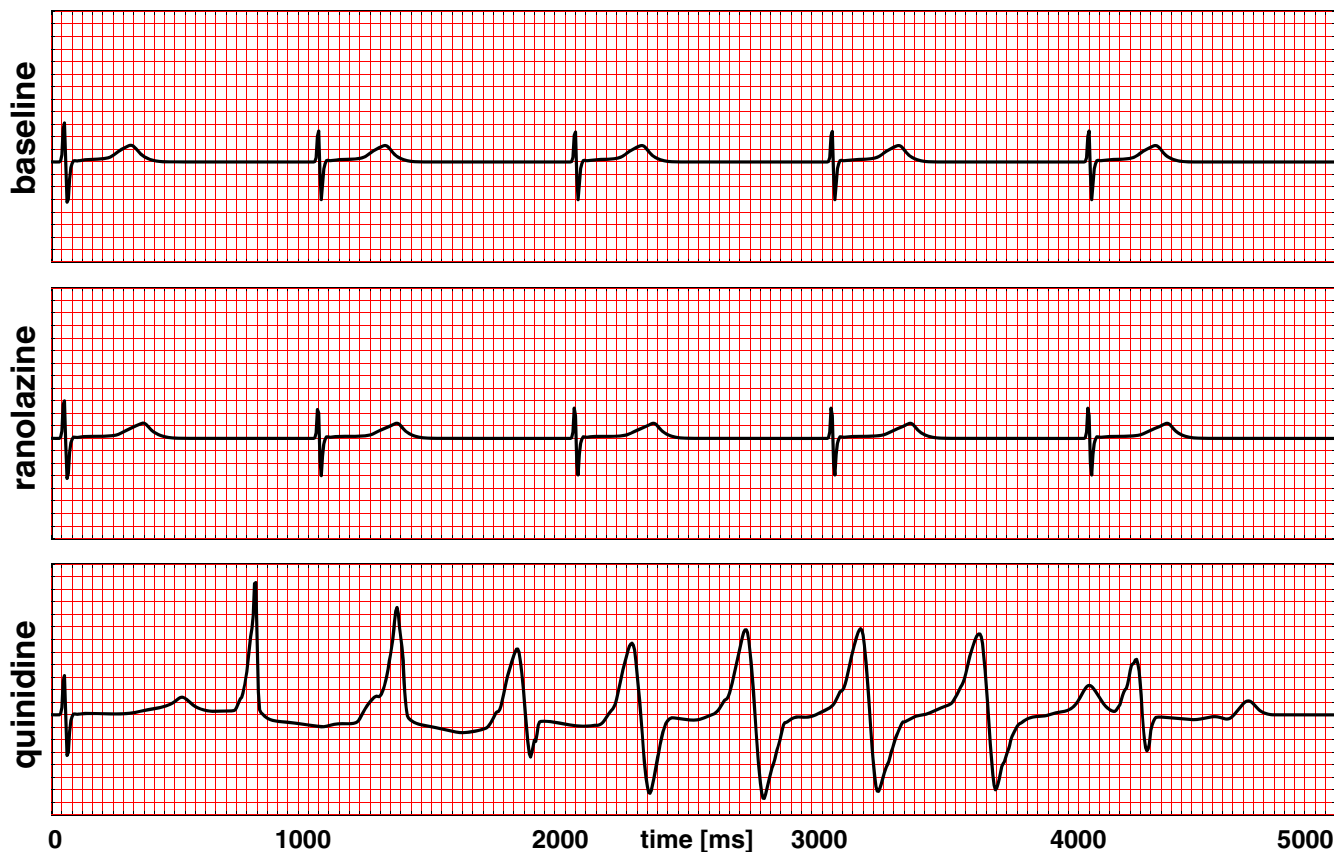


FIGURE 8 Electrocardiogram recordings for baseline and drug treatment with ranolazine and quinidine. Signals are recorded at a precordial lead located 2 cm from the left ventricular wall. The baseline and ranolazine electrocardiograms display regular periodic activation patterns at a heart rate of 60.15 beats per minute determined by the Purkinje fiber network. Ranolazine increases the QT interval by 50.2 milliseconds compared with baseline. The quinidine electrocardiograms displays a regular depolarization during the first 50 milliseconds, followed by a significantly prolonged QT interval, which triggers a sequence of rapid, widened irregular QRS complexes before the heart returns to its regular rhythm, all characteristic features of torsades de pointes

we know that ranolazine slightly prolongs the plateau of the action potential and increases the overall action potential duration. This explains why the repolarization with ranolazine takes 50 milliseconds longer than for the baseline case. Similar to the baseline case, the displayed excitation pattern repeats itself identically every 1000 milliseconds, 5 times within the simulated time window of 5000 milliseconds. Figure 8, middle row, confirms this observation with regular periodic activation patterns and no signs of arrhythmia. The ranolazine electrocardiogram displays a well-defined QRS complex and a positive T wave with a prolonged QT interval of 308.1 milliseconds, an increase of 19.4% compared with the baseline case with no drugs.

Figure 7 illustrates the evolution the transmembrane potential for the case of quinidine. The snapshots are taken at the beginning of the QRS complex at 50 milliseconds, at the end of depolarization at 100 milliseconds, and then at every 1000 milliseconds. During depolarization, from 0 to 100 milliseconds, the Purkinje network drives the excitation from apex to base with a sharp depolarization front propagating across the heart. From Figure 4, right, we know that quinidine has virtually no impact on the upstroke of the single cell action potential during the first 100 milliseconds of the cardiac cycle. This explains why the initial depolarization with quinidine is similar to the cases with no drugs in Figure 5 and with ranolazine in Figure 6. From Figure 4, right, we know that quinidine significantly increases the plateau of the action potential of epicardial cells and, with it, the overall action potential duration. Figure 8, bottom row, illustrates how the prolonged action potential increases the QT interval to 460 milliseconds, an increase of 78.4% compared with the baseline case with no drugs. This initial QT interval of 460 milliseconds is considered a high-risk factor for arrhythmias. Indeed, after 800 milliseconds, the propagation of the excitation wave becomes irregular and asynchronous and the heart is excited in chaotic patterns, from right to left, from base to apex, from left to right, and from apex to base, before the heart seems to return to its regular sinus rhythm after 4200 milliseconds. The rapid, widened irregular QRS complexes patterns that

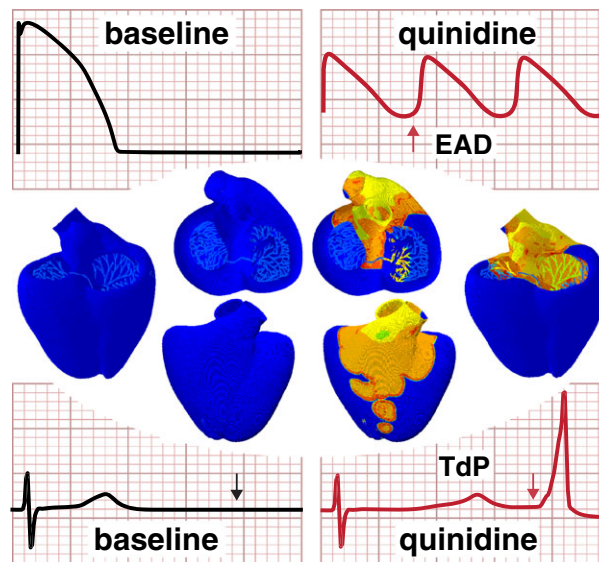


FIGURE 9 Single cell action potentials of midwall cells, excitation profiles at 750 milliseconds, and electrocardiogram recordings of the first 1000 milliseconds for baseline and drug treatment with quinidine. At the single cell level, quinidine induces early afterdepolarizations in midwall cells whose transmembrane potential begins to oscillate around the neutral state. At the organ level, these abnormalities trigger the development of torsades de pointes. Irregular excitation originates in regions with a high density of midwall cells including the basal region near the great vessels, which excites the heart in chaotic patterns

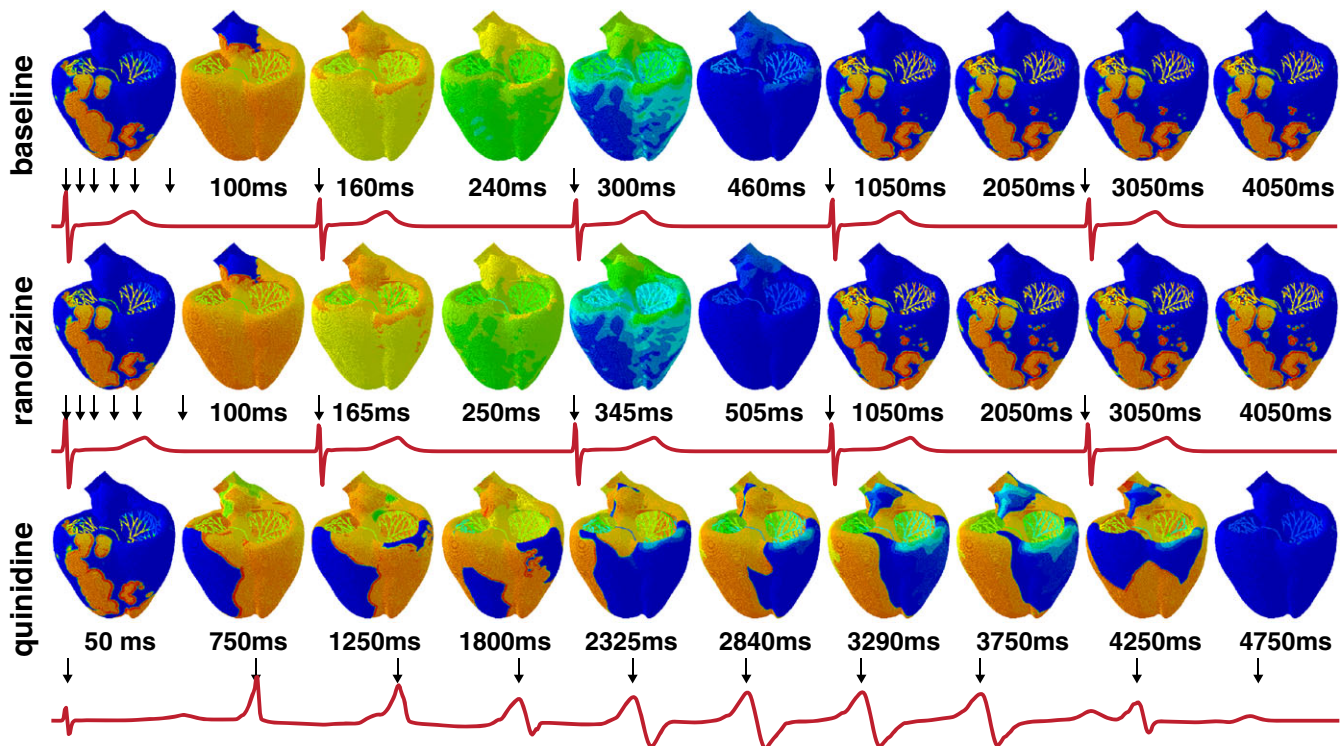


FIGURE 10 Excitation profiles and electrocardiogram recordings for baseline and drug treatment with ranolazine and quinidine. Black arrows in the electrocardiograms indicate the time points of the 10 excitation profiles of each sequence. Compared with baseline with a return to the resting state within 460 milliseconds, drug treatment with ranolazine delays the repolarization period and the return to the resting state takes 505 milliseconds. In both cases, excitation is driven by the Purkinje network, with repeated, similar depolarization patterns every 1000 milliseconds. Drug treatment with quinidine triggers a sequence of rapid, widened irregular QRS complexes with varying activation fronts from right to left, from base to apex, from left to right, and from apex to base, before the heart returns to its resting state at 4750 milliseconds

appear in the electrocardiogram are caused by a ventricular self-excitation that overwrites the regular activation of the Purkinje network, a characteristic hallmark of torsades de pointes.

Figure 9 explains, at least in part, the mechanistic origin of torsadogenesis. In a side-by-side comparison, it summarizes the drug-induced alterations of the single cell action potential of midwall cells, the excitation profiles at 750 milliseconds, and the electrocardiogram recordings of the first 1000 milliseconds for the baseline case, left, and the treatment with quinidine, right. At the single cell level, quinidine induces early afterdepolarizations in midwall cells whose transmembrane potential begins to oscillate closely around the neutral state. At the organ level, regions with a high density of midwall cells, including the basal region near the great vessels, spontaneously overwrite the excitation of the Purkinje fiber network and excite the heart in chaotic patterns. In the electrocardiogram, early afterdepolarizations initiate a drastic peak starting at 750 milliseconds.

Figure 10 summarizes the excitation profiles and electrocardiogram recordings for the baseline case without drugs and drug treatment with ranolazine and quinidine. The black arrows in the electrocardiograms indicate the time points of the 10 excitation profiles of each sequence. Compared with the baseline case with a return to the resting state within 460 milliseconds, drug treatment with ranolazine delays the repolarization period and the return to the resting state takes 505 milliseconds. In both cases, excitation is driven by the Purkinje network, with similar depolarization patterns that repeat themselves every 1000 milliseconds as highlighted in columns 1, 7, 8, 9, and 10. Compared with the baseline case with 5 beats within the simulation window, drug treatment with quinidine spontaneously triggers a sequence of rapid, widened irregular QRS complexes with a total of 9 activation peaks. Characteristic for torsades de pointes, the activation front varies from right to left, from base to apex, from left to right, and from apex to base. After 4750 milliseconds, the heart spontaneously returns to its resting state.

4 | DISCUSSION

The effects of drugs on single cell action potentials have been modeled and simulated extensively throughout the past decade, yet it remains unclear how individual drugs affect the overall excitation pattern of the human heart. A major road block is the required computational power and storage to keep track of the underlying ion channel dynamics across the entire heart. In a collaborative effort, we have created a high-resolution, high-fidelity human heart model with 7 559 760 degrees of freedom and 269 055 341 internal variables to perform simulations throughout a time window of 5000 milliseconds at a spatial and temporal resolution of 0.3 and 0.005 milliseconds. Each simulation runs 40 hours on a 160 processor cluster equipped with Intel Broadwell E5-2683v4 nodes. For postprocessing, we only store the primary degree of freedom, the transmembrane potential at every node, at every 5 milliseconds, which generates an output file of 29 GB. With an element size of 0.3 mm, our simulator has a high enough resolution to accurately capture the electrical wave dynamics. Other recent studies have used resolutions of 0.2,³⁵ 0.4,⁴⁴ and 1.2 mm.⁴¹ We demonstrate the features of our model for the proarrhythmic risk assessment of two representative drugs of low and high risk, ranolazine and quinidine.

For the baseline case without drugs in Figure 5, our model predicts periodic activation patterns with distinct QRS complexes and positive T waves,⁴⁵ which agree well with electrocardiograms of a healthy human heart.⁴⁶ To validate the activation maps themselves, we could, for example, compare Figure 5 with high-resolution electroanatomic mappings of multispine basket catheters.⁴⁷

For the low-risk drug ranolazine in Figure 6, our model predicts periodic activation patterns with a moderate increase of the QT interval, which agrees well with electrocardiograms of ranolazine patients. QT intervals in ranolazine patients have been reported to increase by 6.1 to 9.2 milliseconds¹³ and 5% to 15%⁴⁸ compared with baseline. In ranolazine, two competing effects help explain the moderate prolongation of the QT interval and the low arrhythmic risk: Blocking the rapid delayed rectifier potassium current I_{Kr} increases the QT interval while blocking the late sodium current I_{NaL} decreases it.⁸ From Figure 3, left, we know that the fractional blocks at the free plasma concentration are quite similar, 27.7% for I_{Kr} and 22.2% for I_{NaL} , which could explain why ranolazine mildly affects the QT interval but is classified as a low-risk drug for torsades de pointes.⁴⁹

For the high-risk compound quinidine in Figure 7, our model predicts a significantly prolonged QT interval followed by an episode of torsades de pointes.⁴⁰ Indeed, our initial QT interval of 460 milliseconds is considered a high-risk factor for arrhythmias.⁵⁰ Our results are in line with clinical reports that estimate the frequency of torsades de pointes during quinidine therapy between 2% and 8%.⁵¹ In quinidine, two reinforcing effects help explain the significant prolongation of the QT interval and the high arrhythmic risk: Blocking the rapid and slow delayed rectifier potassium currents I_{Kr} and I_{Ks} significantly increases the QT interval. From Figure 3, right, we know that the fractional blocks at the free plasma

concentration are 71.1% for I_{Kr} and 7.9% for I_{Ks} ,⁵² which explains why quinidine drastically increases the QT interval and is classified as a high-risk drug for torsades de pointes.⁸

With our computational model, we can explain and interpret these electrocardiogram abnormalities by means of the underlying activation patterns in Figures 5 to 7: During torsades de pointes, distinct reentrant waves of ventricular activation overwrite the regular sinus rhythm of the baseline activation in Figure 5. The ventricles re-excite themselves in chaotic patterns with sharp fronts that initiate from the right ventricle, the base, the left ventricle, and the apex, Figure 7, bottom row. As a result, the projection of the heart vector that defines the electrocardiogram trace in Figure 8 displays an irregular sequence of rapid, widened irregular QRS complexes.^{51,53} These observations agree well with simulated reentry patterns in human ventricles in response to drugs,⁵⁴ and with recent simulations of torsades de pointes in heterogeneous ventricles.^{55,56} A unique asset of our multiscale computational model is that these abnormal macroscopic patterns emerge naturally from abnormalities on the microscopic scale. While previous computer models had to initiate reentrant spiral waves *artificially* through an external stimulus in the repolarizing wave tail^{16,54,57,58} or trigger torsades de pointes through external pacing,^{55,56} our model *naturally* predicts the spontaneous transition from a regular rhythm into ventricular tachycardia as a natural consequence of high-risk drugs. Strikingly, our model also predicts a spontaneous termination of the episode of torsades de pointes and a natural return to the resting state.

While our predicted excitation patterns and electrocardiograms agree well with clinical observations, our current study has several limitations that point towards future improvements. In our simulations, first signs of ventricular tachycardia and torsades de pointes were already visible for quinidine at the free plasma concentration. In agreement with the literature,⁵⁹ Figure 9 suggests that early afterdepolarization of midwall cells is a major contributing factor to torsadogenesis. However, recent studies have predicted the development of torsades de pointes for quinidine at normalized concentrations of 10 rather than 1.¹² We attribute this discrepancy to the uncertainty in the current block measurements that critically impact how an individual drug affects the different ion channels in Figure 3. In a current follow-up study, we are currently characterizing the effects of current block variations using uncertainty quantification. This will provide a range of QT intervals for any given drug, which will allow us to better estimate the risk of torsades de pointes.

After thorough experimental validation—for example, with the rich data sets provided by the CiPA initiative—we believe that our multiscale model can become a critical tool for proarrhythmic risk assessment. Our exposure-response simulation allows us to virtually probe the effects of different current blocks—combined and in isolation—on the development of torsades de pointes. Computational sensitivity analyses can reveal how individual currents interact with one another and help prioritize selective channel blocks during drug development. These new mechanistic insights will help researchers, regulatory agencies, and pharmaceutical companies to accelerate drug development and create effective and safe drugs.

ACKNOWLEDGMENTS

This model was developed within the Living Heart project. We acknowledge the Zygote Media Group for providing the anatomic model and Dassault Systèmes SIMULIA, Uber Cloud, Advania, and Hewlett Packard Enterprise for providing the computational resources for our simulations. This study was supported by a Stanford Cardiovascular Institute seed grant and by the Becas Chile-Fulbright Fellowship to Francisco Sahli Costabal and by the National Institutes of Health grant U01 HL119578 to Ellen Kuhl.

ORCID

Ellen Kuhl  <http://orcid.org/0000-0002-6283-935X>

REFERENCES

1. Dessertenne F. La tachycardie ventriculaire a deux foyers opposes variables. *Arch Mal Coeur Vaiss*. 1966;2(59):263-272.
2. Po SS, Wang DW, Yang IC, Johnson JP, Nie L, Bennett PB. Modulation of HERG potassium channels by extracellular magnesium and quinidine. *J Cardiovasc Pharmacol*. 1999;33(2):181-185.
3. Redfern WS, Carlsson L, Davis AS, et al. Relationships between preclinical cardiac electrophysiology, clinical QT interval prolongation and torsade de pointes for a broad range of drugs: evidence for a provisional safety margin in drug development. *Cardiovasc Res*. 2003;58(1):32-45.
4. Gintant G, Sager PT, Stockbridge N. Evolution of strategies to improve preclinical cardiac safety testing. *Nat Rev Drug Discov*. 2016;15(7):1-15.

5. Navarrete EG, Liang P, Lan F, et al. Screening drug-induced arrhythmia using human induced pluripotent stem cell-derived cardiomyocytes and low-impedance microelectrode arrays. *Circulation*. 2013;128:S3-S13.
6. Sager PT, Gintant G, Turner JR, Pettit S, Stockbridge N. Rechanneling the cardiac proarrhythmia safety paradigm: a meeting report from the Cardiac Safety Research Consortium. *Am Heart J*. 2014;167(3):292-300.
7. Chabiniok R, Wang V, Hadjicharalambous M, et al. Multiphysics and multiscale modeling, data-model fusion and integration of organ physiology in the clinic: ventricular cardiac mechanics. *Interface Focus*. 2016;6:20150083.
8. Colatsky T, Fermini B, Gintant G, et al. The comprehensive in vitro proarrhythmia assay (CiPA) initiative – Update on progress. *J Pharmacol Toxicol Methods*. 2016;81:15-20.
9. Mirams GR, Cui Y, Sher A, et al. Simulation of multiple ion channel block provides improved early prediction of compounds' clinical torsadogenic risk. *Cardiovasc Res*. 2011;91(1):53-61.
10. Obiol-Pardo C, Gomis-Tena J, Sanz F, Saiz J, Pastor M. A multiscale simulation system for the prediction of drug-induced cardiotoxicity. *J Chem Inf Model*. 2011;51(2):483-492.
11. Beattie KA, Luscombe C, Williams G, et al. Using ion channel screening data to predict QT interval changes in the rabbit ventricular wedge. *J Pharmacol Toxicol Methods*. 2013;68(1):88-96.
12. Okada J, Yoshinaga T, Kurokawa J, et al. Screening system for drug-induced arrhythmogenic risk combining a patch clamp and heart simulator. *Sci Adv*. 2015;1(4):e1400142-e1400142.
13. Chaitman BR. Ranolazine for the treatment of chronic angina and potential use in other cardiovascular conditions. *Circulation*. 2006;113:2462-2472.
14. Crumb WJ, Vicente J, Johannesen L, Strauss DG. An evaluation of 30 clinical drugs against the comprehensive in vitro proarrhythmia assay (CiPA) proposed ion channel panel. *J Pharmacol Toxicol Methods*. 2016;81:251-262.
15. Wenckebach KF. *Die unregelmässige Herztätigkeit und ihre klinische Bedeutung*. Leipzig und Berlin: Wilhelm Engelmann; 1914.
16. Krishnamoorthi S, Perotti LE, Borgstrom NP, et al. Simulation methods and validation criteria for modeling cardiac ventricular electrophysiology. *PLoS ONE*. 2014;9(12):e114494.
17. Niederer S, Kerfoot E, Benson AP, et al. Verification of cardiac tissue electrophysiology simulators using an N-version benchmark. *Philos Trans Ser A Math Phys Eng Sci*. 2011;369(1954):4331-51.
18. Göktepe S, Kuhl E. Computational modeling of cardiac electrophysiology: a novel finite element approach. *Int J Numer Meth Eng*. 2009;79(2):156-178.
19. Keener J, Sneyd J. *Mathematical Physiology II: Systems Physiology*. New York: Springer; 2009.
20. Lee LC, Sundnes J, Genet M, Wenk JF, Wall ST. An integrated electromechanical-growth heart model for simulating cardiac therapies. *Biomech Model Mechanobiol*. 2016;15(4):791-803.
21. Wong J, Göktepe S, Kuhl E. Computational modeling of chemo-electro-mechanical coupling: a novel implicit monolithic finite element approach. *Int J Numer Method Biomed Eng*. 2013;29:1104-1133.
22. O'Hara T, Virág L, Varró A, Rudy Y. Simulation of the undiseased human cardiac ventricular action potential: model formulation and experimental validation. *PLOS Comput Biol*. 2011;7(5):e1002061.
23. Dutta S, Chang KC, Beattie KA, et al. Optimization of an in silico cardiac cell model for proarrhythmia risk assessment. *Front Physiol*. 2017;8:1-15.
24. ten Tusscher KH, Noble D, Noble PJ, Panfilov AV. A model for human ventricular tissue. *Am J Physiol Heart Circ Physiol*. 2004;286(4):H1573-89.
25. Priest JR, Gawad C, Kahlig KM, et al. Early somatic mosaicism is a rare cause of long-QT syndrome. *Proc Natl Acad Sci*. 2016;113(41):115550-11560.
26. Stewart P, Aslanidi OV, Noble D, Noble PJ, Boyett MR, Zhang H. Mathematical models of the electrical action potential of Purkinje fibre cells. *Philos Trans Math Phys Eng Sci*. 2009;367(1896):2225-2255.
27. O'Hara T, Virág L, Varró A, Rudy Y. ORd original human ventricular model. <http://ignorespaces//rudylab.wustl.edu/research/cell/code/AllCodes.html> Accessed January 1, 2017; 2011.
28. Stewart P, Aslanidi OV, Noble D, Noble PJ, Boyett MR, Zhang H. Mathematical models of the electrical action potential of Purkinje fibre cells. <https://models.cellml.org> Accessed January 1, 2017; 2009.
29. Dassault Systèmes, SIMULIA. *Abaqus 2017, Documentation*. Rhode Island: Dassault Systèmes; 2017.
30. Krishnamoorthi S, Sarkar M, Klug WS. Numerical quadrature and operator splitting in finite element methods for cardiac electrophysiology. *Int J Numer Method Biomed Eng*. 2013;29:1243-1266.
31. Group ZM. *Zygote Solid 3d Heart Generations I & II Development Report, Technical Development of 3D Anatomical Systems*; 2014.
32. Rausch M, Zöllner AM, Genet M, Baillargeon B, Bothe W, Kuhl E. A virtual sizing tool for mitral valve annuloplasty. *Int J Numer Method Biomed Eng*. 2017;33:e02788.
33. Baillargeon B, Rebelo N, Fox DD, Taylor RL, Kuhl E. The living heart project: a robust and integrative simulator for human heart function. *European J Mech A Solids*. 2014;48:38-47.
34. Perotti LE, Krishnamoorthi S, Borgstrom NP, Ennis DB, Klug WS. Regional segmentation of ventricular models to achieve repolarization dispersion in cardiac electrophysiology modeling. *Int J Numer Method Biomed Eng*. 2015;28:e02718.
35. Okada J, Washio T, Maehara A, Momomura S, Sugiura S, Hisada T. Transmural and apicobasal gradients in repolarization contribute to T-wave genesis in human surface ECG. *Am J Physiol Heart Circ Physiol*. 2011;301(1):H200-H208.
36. Sahli Costabal F, Hurtado DE, Kuhl E. Generating Purkinje networks in the human heart. *J Biomech*. 2016;49:2455-2465.

37. Ponnaluri AVS, Perotti LE, Ennis DB, Klug WS. A viscoactive constitutive modeling framework with variational updates for the myocardium. *Comput Meth Appl Mech Eng*. 2016;314:85-101.
38. Bordas R, Gillow K, Lou Q, et al. Rabbit-specific ventricular model of cardiac electrophysiological function including specialized conduction system. *Prog Biophys Mol Biol*. 2011;107(1):90-100.
39. Kotikanyadanam M, Göktepe S, Kuhl E. Computational modeling of electrocardiograms: a finite element approach toward cardiac excitation. *Int J Numer Method Biomed Eng*. 2010;26(5):524-533.
40. Hii JTY, Wyse G, Gillis AM, Duff HJ, Solylo MA, Mitchell LB. Precordial qt interval dispersion as a marker of Torsade de Pointes. *Circulation*. 1992;86:1376-1382.
41. Sadrieh A, Domanski L, Pitt-Francis J, et al. Multiscale cardiac modelling reveals the origins of notched T waves in long QT syndrome type 2. *Nat Commun*. 2014;5:5069.
42. Ju YK, Saint DA, Gage PW. Effects of lignocaine and quinidine on the persistent sodium current in rat ventricular myocytes. *Br J Pharmacol*. 1992;107:311-316.
43. Kramer J, Obejero-Paz CA, Myatt G, et al. MICE models: superior to the HERG model in predicting Torsade de Pointes. *Sci Rep*. 2013;3:2100.
44. Dutta S, Mincholé A, Zacur E, Quinn TA, Taggart P, Rodriguez B. Early afterdepolarizations promote transmural reentry in ischemic human ventricles with reduced repolarization reserve. *Prog Biophys Mol Biol*. 2016;120:236-248.
45. Hurtado DE, Kuhl E. Computational modelling of electrocardiograms: repolarisation and T-wave polarity in the human heart. *Comput Meth Biomech Biomed Eng*. 2014;17(9):986-996.
46. Schenone E, Collin A, Gerbeau JF. Numerical simulation of electrocardiograms for full cardiac cycles in healthy and pathological conditions. *Int J Numer Method Biomed Eng*. 2016;32:e02744.
47. Tanaka Y, Genet M, Lee LC, Martin AJ, Sievers R, Gerstenfeld EP. Utility of high-resolution electroanatomic mapping of the left ventricle using a multispline basket catheter in a swine model of chronic myocardial infarction. *Heart Rhythm*. 2015;1(12):144-154.
48. Johannesen L, Vicente J, Mason JW, et al. Differentiating drug-induced multichannel block on the electrocardiogram: randomized study of dofetilide, quinidine, ranolazine, and verapamil. *Clin Pharmacol Ther*. 2014;96(5):549-58.
49. Antzelevitch C, Belardinelli L, Zygmunt AC, et al. Electrophysiological effects of ranolazine, a novel antianginal agent with antiarrhythmic properties. *Circulation*. 2004;110(8):904-910.
50. Yap YG, Camm AJ. Drug induced QT prolongation and torsades de pointes. *Heart*. 2003;89(11):1363-1372.
51. Viskin S. Long qt syndromes and torsade de pointes. *Lancet*. 1999;354:1625-1633.
52. Hurtado DE, Castro S, Madrid P. Uncertainty quantification of 2 models of cardiac electromechanics. *Int J Numer Method Biomed Eng*. 2017. <https://doi.org/10.1002/cnm.2894>.
53. Krikler DM, Curry PVL. Torsade de pointes, an atypical ventricular tachycardia. *Br Heart J*. 1976;38:117-120.
54. Moreno JD, Zhu ZI, Yang P, et al. A computational model to predict the effects of class I anti- arrhythmic drugs on ventricular rhythms. *Sci Transl Med*. 2011;3(98):1-20.
55. Vandersickel N, de Boer TP, Vos MA, Panfilov AV. Perpetuation of torsade de pointes in heterogeneous hearts: competing foci or re-entry. *J Physiol*. 2016;594:6865-6878.
56. Vandersickel N, Van Nieuwenhuysse E, Seemann G, Panfilov AV. Spatial patterns of excitation at tissue and whole organ level due to early afterdepolarizations. *Front Physiol*. 2017;8:404.
57. Göktepe S, Wong J, Kuhl E. Atrial and ventricular fibrillation: computational simulation of spiral waves in cardiac tissue. *Arch Appl Mech*. 2010;80(5):569-580.
58. Sahli Costabal F, Zaman JAB, Kuhl E, Narayan SM. Interpreting activation mapping of atrial fibrillation: a hybrid computational/physiological study. *Ann Biomed Eng*. 2018;46:257-269.
59. Antzelevitch C, Sicouri S. Clinical relevance of cardiac arrhythmias generated by afterdepolarizations: role of M cells in the generation of U waves, triggered activity and torsade de pointes. *J Am Coll Cardiol*. 1994;23:259-277.

How to cite this article: Sahli Costabal F, Yao J, Kuhl E. Predicting drug-induced arrhythmias by multiscale modeling. *Int J Numer Meth Biomed Engng*. 2018;34:e2964. <https://doi.org/10.1002/cnm.2964>